A&A, 691, A329 (2024)
https://doi.org/10.1051/0004-6361/202451172

Astronomy & Astrophysics

Multi-wavelength observations of the luminous fast blue optical transient AT 2023fhn

Up to ~200 days post-explosion

A. A. Chrimes[1,2,⋆,⋆⋆], D. L. Coppejans[3], P. G. Jonker[2], A. J. Levan[2,3], P. J. Groot[2,4,5], A. Mummery[6], and E. R. Stanway[3]

[1] European Space Agency (ESA), European Space Research and Technology Centre (ESTEC), Keplerlaan 1, 2201 AZ Noordwijk, The Netherlands
[2] Department of Astrophysics/IMAPP, Radboud University, PO Box 9010, 6500 GL, Nijmegen, The Netherlands
[3] Department of Physics, University of Warwick, Gibbet Hill Road, CV4 7AL Coventry, UK
[4] Inter-University Institute for Data Intensive Astronomy, Department of Astronomy, University of Cape Town, Private Bag X3, Rondebosch 7701, South Africa
[5] South African Astronomical Observatory, P.O. Box 9, 7935 Observatory, South Africa
[6] Oxford Astrophysics, Denys Wilkinson Building, Keble Road, Oxford OX1 3RH, UK

Received 19 June 2024 / Accepted 21 October 2024

ABSTRACT

Context. Luminous fast blue optical transients (LFBOTs) are a class of extragalactic transients notable for their rapid rise and fade times, blue colour, and accompanying luminous X-ray and radio emission. Only a handful have been studied in detail since the prototypical example AT 2018cow. Their origins are currently unknown, but ongoing observations of previous and new events are placing ever stronger constraints on their progenitors.
Aims. We aim to put further constraints on the LFBOT AT 2023fhn, and LFBOTs as a class, using information from the multi-wavelength transient light curve, its host galaxy, and local environment.
Methods. Our primary results were obtained by fitting galaxy models to the spectral energy distribution of AT 2023fhn's host and local environment, and by modelling the radio light curve of AT 2023fhn as due to synchrotron self-absorbed emission from an expanding blast wave in the circumstellar medium.
Results. We find that neither the host galaxy nor circumstellar environment of AT 2023fhn are unusual compared with previous LFBOTs, but that AT 2023fhn has a much lower X-ray to ultraviolet luminosity ratio than previous events.
Conclusions. We argue that the variety in ultraviolet-optical to X-ray luminosity ratios among LFBOTs is likely due to viewing angle differences, and that the diffuse, yet young local environment of AT 2023fhn – combined with a similar circumstellar medium to previous events – favours a progenitor system containing a massive star with strong winds. Plausible progenitor models in this interpretation therefore include the mergers of black holes and Wolf-Rayet stars or failed supernovae.

Key words. black hole physics – stars: black holes – circumstellar matter – supernovae: general – stars: winds, outflows – supernovae: individual: AT 2023fhn

1. Introduction

Luminous fast blue optical transients (LFBOTs) are a rare class of rapidly evolving, hot, multi-wavelength extragalactic transients. The prototypical example, AT 2018cow ('the Cow', Prentice et al. 2018), is the nearest and best-studied event of this class so far. Its characteristic early-time features include a peak optical absolute magnitude of ~–20 with a rapid rise and decay timescale of ~5 days, constraining the ^{56}Ni mass in the ejecta to <0.004 $M_\odot$, and ruling out standard core-collapse or thermonuclear supernova models (Perley et al. 2019; Margutti et al. 2019). The optical-ultraviolet (UV) emission is well fit by a hot black-body and power-law component, where the black-body temperature was $\sim 3\times10^4$ K initially, falling to $\sim 1.5\times10^4$ K over two weeks (Prentice et al. 2018; Perley et al. 2019). The optical spectra were largely featureless, with broad hydrogen absorption features (indicative of a high outflow velocity) appearing and disappearing between 2–8 days, and narrow He lines appearing after ~20 days. At other wavelengths, AT 2018cow was X-ray and radio bright (Rivera Sandoval et al. 2018; Margutti et al. 2019; Ho et al. 2019; Nayana & Chandra 2021). The X-ray emission was well in excess of power-law extrapolations from the radio (e.g. Ho et al. 2019) and was also highly variable after a break in the light curve, which declined as $L \propto t^{-2}$ after ~20 days (Migliori et al. 2024). The broadband X-ray spectrum and X-ray variability cannot be explained by an external shock origin, and the synchrotron self-absorbed radio emission – consisting of a slow rise and rapid decay – was instead smoothly evolving, indicating a distinct physical origin from the highly variable X-rays. An interpretation is that a central engine powers the X-ray emission, while an expanding blast wave produces the radio emission (e.g. Ho et al. 2019; Margutti et al. 2019). The slow radio variability timescale set the size of the emission region at

⋆ Corresponding author; ashley.chrimes@esa.int
⋆⋆ ESA Research Fellow.

5–6 days at $<3 \times 10^{15}$ cm, while the X-ray variability gave a length scale approximately five times smaller (Ho et al. 2019). Therefore, the X-rays appear to originate from a central engine or internal shock, while the radio emission is generated externally. A claim of quasi-periodic oscillations in the X-rays can be interpreted as evidence for a $<850\,M_\odot$ central engine (Pasham et al. 2021), while a separate claim of ∼250 s quasi-periodicity instead implies an intermediate-mass (10^3–10^5 $M_\odot$) black hole (IMBH) (Zhang et al. 2022). Synchrotron modelling of the sub-millimetre and radio data revealed a mildly relativistic expansion velocity ($\sim 0.1c$) into a wind-like extended circumstellar medium (CSM) with a high density of $\sim 10^5$ cm^{-3} (Margutti et al. 2019; Ho et al. 2019). For Wolf-Rayet-like wind speeds of ∼1000 km s^{-1}, this implies a mass-loss rate $\dot{M} = 10^{-4}$–$10^{-3}\,M_\odot$ yr^{-1} (Margutti et al. 2019).

Since AT 2018cow, several more LFBOTs have been discovered. Confirmed events include AT 2018lug/ZTF 18abvkwla ('the Koala', Ho et al. 2020), CSS161010 (Coppejans et al. 2020), AT 2020xnd/ZTF 20 acigmel ('the Camel', Perley et al. 2021; Bright et al. 2022; Ho et al. 2022), AT 2020mrf (Yao et al. 2022), AT 2022tsd ('the Tasmanian Devil', Matthews et al. 2023), and AT 2023fhn ('the Finch', Chrimes et al. 2024). Despite variety (e.g. in peak luminosity), they share the same key features of hot, largely featureless spectra at early times, optical luminosities rivalling superluminous supernovae, plus bright X-ray and radio emission. They are estimated to occur at <0.1% of the local core-collapse supernova rate (Ho et al. 2023a).

Recent developments have provided further insight into the origin of LFBOTs. Polarimetry of AT 2018cow demonstrated the emission region to be highly aspherical, indicative of an accretion disc (Maund et al. 2023). Unexpectedly, AT 2018cow was found to be UV (Sun et al. 2022, 2023; Chen et al. 2023; Inkenhaag et al. 2023) and X-ray (Migliori et al. 2024) bright at late times, several years post-explosion. This emission has been interpreted as from a black hole accretion disc. Estimates for the black hole mass range from ∼10–100 $M_\odot$ (super-Eddington accretion) to ∼10^3–10^4 $M_\odot$ (sub-Eddington, from X-ray observations, Migliori et al. 2024) and ∼1000 $M_\odot$ (UV observations, Inkenhaag et al. 2023). Magnetar central engine models struggle to produce both the early and late UV emission (Chen et al. 2023). Further evidence for a black hole accretion scenario comes from minute-long optical flares, up to several months post-explosion, from AT 2022tsd (Ho et al. 2023b). An interpretation is that the central engine is undergoing highly variable, short-lived bursts of accretion.

Several models have been put forward to explain LFBOTs. Tidal disruptions of compact, hydrogen-poor stars (such as white dwarfs) around IMBHs can plausibly explain the optical rise and fall timescale, spectral features, and X-ray variability timescale (Perley et al. 2019; Kuin et al. 2019). However, the dense CSM inferred from radio observations is hard to explain in such a scenario (e.g. Margutti et al. 2019). Other possibilities include failed supernovae, in which a black hole is formed and the emission is powered by accretion onto the natal black hole rather than radioactive decay in the ejecta (Perley et al. 2019; Quataert et al. 2019), choked jets (e.g. Gottlieb et al. 2022; Soker 2022), highly aspherical supernovae ('ellipsars', DuPont et al. 2022), and the mergers of compact objects and/or massive stars (Lyutikov & Toonen 2019; Uno & Maeda 2020; Schrøder et al. 2020), such as black holes and Wolf-Rayet stars (Metzger 2022). A dense outflow from the progenitor may result in dust echoes (Metzger & Perley 2023). CSM shock interaction models have also been put forward (e.g. Fox & Smith 2019; Xiang et al. 2021; Pellegrino et al. 2022; Khatami & Kasen 2024), but the X-ray variability, broadband spectral evolution, late-time UV/X-ray emission from AT 2018cow, and giant optical flares from AT 2022tsd all indicate the presence of a central engine.

In this paper, we present multi-wavelength radio, optical, UV, and X-ray observations of the LFBOT AT 2023fhn up to ∼200 days post-explosion. We place AT 2023fhn in the context of other LFBOTs so far, in terms of its host galaxy, optical/UV/X-ray light curve, and radio emission, with the event energetics and blast-wave properties inferred from synchrotron modelling of the radio observations. Throughout, we use a flat ΛCDM cosmology with $\Omega_m = 0.3$ and $H_0 = 70$ kms^{-1} Mpc^{-1}. All magnitudes are reported in the AB system (Oke & Gunn 1982).

2. Observations and data reduction

2.1. X-ray

We obtained four epochs of Chandra X-ray Observatory ACIS-S observations of AT 2023fhn up to ∼200 days post-explosion. The epochs consist of 1, 2, 6 and 14 observations, respectively (full details are provided in Table A.1). The data are reduced, and transient fluxes measured, with standard CIAO (v4.13, caldb v4.9.3, Fruscione et al. 2006) procedures. The images are reprocessed and filtered to the energy range 0.5–7.0 keV. WAVDETECT is used to find point sources, and SRCFLUX used to measure the flux (or upper limits) at the location of AT 2023fhn. We merged the datasets in each of the four epochs (with MERGE_OBS) to increase the signal-to-noise ratio. The mean (mid-point, exposure-time weighted) observation times of these epochs are 15.0, 28.9, 64.5 and 210.9 days (since JD–2460045, or 12:00 UT on 10-Apr-2023). The total exposure times per epoch are ∼30, 60, 83 and 193 ks respectively. Finally, the fluxes are de-absorbed by assuming a photon index $\Gamma = 2$ (e.g. Rivera Sandoval et al. 2018), and a Galactic neutral hydrogen column density of $N_H = 2.78 \times 10^{20}$ cm^{-2} (Dickey & Lockman 1990).

2.2. UV-optical

A second epoch of *Hubble* Space Telescope (HST) imaging was obtained on 23/24 October 2023 (the first was on 17 May 2023, Chrimes et al. 2024), using the WCF3 instrument and six filters (F225W, F336W, F555W, F763M, F814W, F845M). Full details are given in Table A.2. The data are reduced with DRIZZLEPAC (Hoffmann et al. 2021), re-drizzling the charge-transfer-efficiency-corrected _FLC input images with north oriented up and a final pixel scale of 0.025 arcsec pixel^{-1} (PIXFRAC = 0.8). Image stamps around the location of AT 2023fhn in epochs 1 and 2 are shown in Fig. 1. Visible in the bottom left is the presumed satellite of the larger spiral to the south (see Fig. 2). Both galaxies lie at a common redshift of ∼0.24 (Ho et al. 2023c; Chrimes et al. 2024).

2.3. Radio

We obtained radio observations with the *Karl G. Jansky* Very Large Array (VLA) between 22 Apr 2023 and 16 December 2024 (program SC240143, PI: Chrimes). Details of the observations are listed in Table A.3. The observations were taken in standard phase-referencing mode using 3C 286 as a flux density and bandpass calibrator, with ICRF J101447.0+230116, FIRST J101644.3+203747, FIRST J101353.4+244916 and ICRF J095649.8+251516 as complex gain calibrators. The observations were calibrated

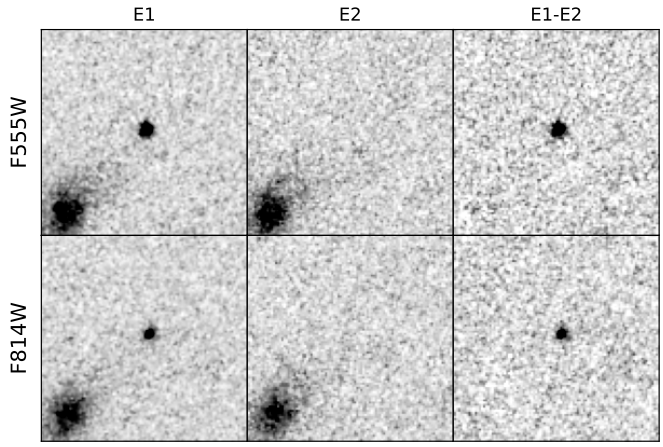

Fig. 1. F555W and F814W HST/WFC3 image stamps at the location of AT 2023fhn in the first epoch (May 2023, left) and the second epoch (October 2023, centre). The right-hand panels show difference images (epoch 1 – epoch 2). North is up, east is left, and the stamps are 2.5 arcsec on each side.

using the VLA Calibration Pipeline versions 2023.1.0.124 and 2022.2.0.64 in CASA v6.5.4 and v6.4.1 respectively, with additional manual flagging. The images were created using the TCLEAN task in CASA with Briggs weighting with a robust parameter of 1. In the observations where the source was not detected we quote the upper limit on the flux density as three times the local root mean square (RMS). The one exception to this is during the last epoch (see Table A.3) where the synthesised beam (resolution element) was large and included other sources. In this case we quoted the upper limit as the flux density at the source location. For the observations where we detected the target, we fitted the flux density using the imfit task within CASA and constrained the fit to the synthesised beam.

The observations up to ∼12 days post JD-2460045 are already published (Chrimes et al. 2024) and all produced non-detections. In the ∼87–95 day and ∼138 day epochs we have sufficient data points for fitting a synchrotron self-absorbed spectrum. The K_U band (15 GHz) data point at 138 days has sufficient signal-to-noise to split into 3 (centred on 13, 15 and 17 GHz), as listed in Table A.3, increasing the points at ∼138 days to 7 (with 6 detections). We fit a self-absorbed synchrotron model to the ∼87–95 and ∼138 day epochs in Sect. 4.4.

3. Environmental analysis

3.1. Local environment

The second epoch of HST imaging presented in this paper allows us to examine the environment directly underlying the transient after it has faded. As noted by Chrimes et al. (2024), there is diffuse emission in the vicinity of the transient. To characterise this faint underlying population, we place 0.2 arcsec (and 0.4 arcsec) apertures at the location of AT 2023fhn in all six epoch two images. The images are aligned with x–y shifts using five common point sources in every image, with respect to the location of AT 2023fhn in the epoch 1 F555W image. The RMS of these relative astrometric alignments is ∼5–10 mas, better than the absolute astrometry of the images (which have been aligned with the *Gaia* DR3 reference frame), and much smaller than the aperture size. We perform photometry with PHOTUTILS, estimating the background with either the median image background (with MEDIANBACKGROUND) or an annulus (1.5 to 4 times the aperture radius, with pixels values clipped at 3σ). The appropriate encircled energy corrections for each filter and aperture are applied. Magnitudes are then calculated using the PHOTPLAM and PHOTFLAM header keywords[1], and are listed in Table A.4. The only detections are in F555W and F814W. To investigate the nature of these detections, we place eight 0.4 arcsec apertures at equal spacing around the location of AT 2023fhn in a circle of radius 20 pixels (0.5 arcsec). With the F555W filter and median background subtraction, we have significant detections in 5/8 apertures, with a mean magnitude of 25.9 ± 0.6 in these apertures – consistent with the measurement at the precise location of AT 2023fhn. This demonstrates that the emission in this area is from an extended, diffuse background, rather than any significant contribution by residual light from AT 2023fhn. This can also be seen in Table A.4, where the magnitudes calculated with annulus background subtraction are fainter, since the local background is elevated. Larger apertures also give brighter magnitudes, despite encircled energy correction (unlike point sources in the field). For this reason, we exclusively use median background subtracted measurements – which are not biased by the nearest pixels in the image – in the following analysis.

We disfavour a significant contribution from a compact cluster at this specific location, which would appear as a point source in the image given the physical scale at this redshift of ∼100 pc pixel^{-1}. However, the presence of a globular cluster (which would favour an IMBH interpretation, e.g. Lützgendorf et al. 2013) cannot be ruled out, as even the brightest globular clusters would be far below detection limits at this distance and limiting magnitude (Chrimes et al. 2024). Shifting the circle of apertures 5 arcsec to the north, well away from the galaxies, we find non-detections in all eight apertures with a 3σ upper limit of 26.7. We therefore conclude that there is extended, diffuse emission from an underlying stellar population at the location of AT 2023fhn.

We now estimate the age and dust extinction of this underlying population. First, we correct for the (low) Galactic extinction of $E(B-V) = 0.0254$ (Schlafly & Finkbeiner 2011)[2] using the filter effective wavelengths (Rodrigo et al. 2012; Rodrigo & Solano 2020) and the Python EXTINCTION package (Barbary 2016) with a Fitzpatrick (1999) extinction law and $R_V = 3.1$. To estimate the age and local (intrinsic) extinction, we fit the Galactic-extinction corrected F225W, F336W, F555W and F814W photometry (both 0.2 and 0.4 arcsec apertures, median background subtracted) to BPASS (Binary Population and Spectral Synthesis v2.1, Eldridge et al. 2017; Stanway & Eldridge 2018) single-age spectral templates. These are constructed by assuming that a stellar population of 10^6 $M_\odot$ is formed instantaneously, and left to evolve with no further star formation. We use these simple stellar populations since the limited data available to model solely the local environment of AT 2023fhn precludes a more complex procedure, including, for example, the star-formation history (however, see the next section). A fixed metallicity of half-Solar is adopted ($Z = 0.01$ by mass fraction). We therefore simply fit for the age of the population, the luminosity (i.e. mass) of the stellar population is then allowed to freely vary to minimise χ^2. Four data points are used (F225W, F336W, F555W and F814W). Formal flux measurements are used for F225W and F336W; these produce magnitudes of $29.0^{+1.7}_{-2.0}$ and $27.3^{+0.6}_{-1.4}$ respectively (with a 0.2 arcsec aperture) and $26.9^{+0.7}_{-1.0}$ and $26.7^{+0.6}_{-1.8}$ (with a 0.4 arcsec aperture). We therefore have 2

[1] https://hst-docs.stsci.edu/wfc3dhb/chapter-9-wfc3-data-analysis/9-1-photometry
[2] https://irsa.ipac.caltech.edu/applications/DUST/

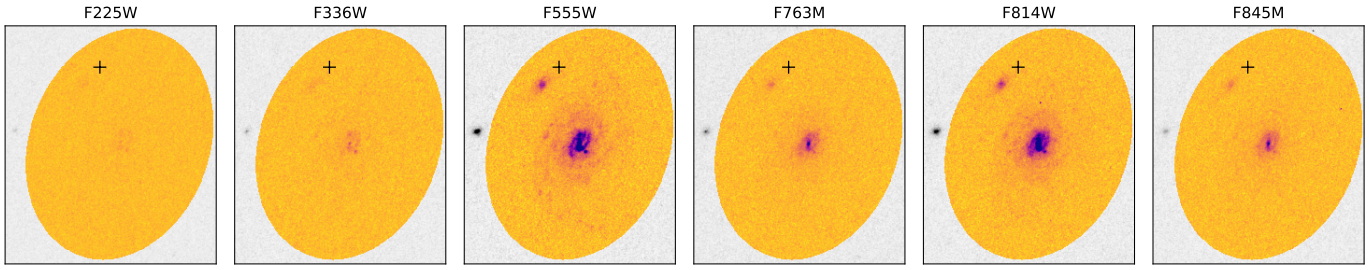

Fig. 2. HST imaging of the galaxy hosting AT 2023fhn in the six epoch 2 filters. Pixels within 1.5 $R_{\rm petro}$ of the spiral galaxy centroid are selected as associated with the host, and given an orange-purple colourmap (see text for details). This region fully encompasses the satellite galaxy. The location of AT 2023fhn is marked with a + sign. The image cutouts are 13 arcsec on each side. North is up and east is left.

fit parameters and 4 data points for 2 degrees of freedom. Fitting is performed by multiplying the (de-redshifted) filter response curves (Rodrigo et al. 2012; Rodrigo & Solano 2020) with the BPASS spectra to extract fluxes and hence magnitudes from the spectra. These are compared with the absolute magnitudes in each filter, after correction for a range of intrinsic extinction values from $A_{\rm V}$ = 0.0 to 4.0. The intrinsic extinction correction uses the rest-frame effective wavelength of each filter. The F763M and F845M filters are not used in this fit since the upper limits are shallower than the F555W and F814W detections, and so provide no additional constraints.

The results are shown in Fig. 3. The left-hand panels show the best-fit single-age BPASS spectra. The right-hand panels show $\log_{10}(\chi^2)$ across the parameter space. Each pixel represents a unique combination of $A_{\rm V}$ and a BPASS simple stellar population at a given age. The 68% and 90% confidence intervals are indicated by crosses and dots respectively (where the $\Delta\chi^2$ intervals are from Avni 1976). We can see that the choice of a 0.2 or 0.4 arcsec aperture makes little difference, likely because the increased aperture size simply captures more of the same diffuse background light at that position, without changing the colours significantly. In both cases, there is a degeneracy between age and extinction, and while the uncertainties are large, population ages in excess of a few hundred Myr are disfavoured. The range of possible ages for this diffuse emission is therefore broadly consistent with the core-collapse supernova delay time distribution (e.g. Eldridge et al. 2019).

We also measure the local surface brightness in epoch 2 (in a 0.5 arcsec radius around AT 2023fhn's position), giving 25.1 mag arcsec^{-2} in F555W and 24.65 mag arcsec^{-2} in F814W. This compares well with the 25.2 mag arcsec^{-2} and 24.6 mag arcsec^{-2} values from the transient-subtracted images in Epoch 1 (see Chrimes et al. 2024). The F336W surface brightness is 25.76 mag arcsec^{-2}, which after Galactic extinction correction is 25.27 mag arcsec^{-2}. The rest-frame central wavelength of F336W is ∼2700 Å. This allows for a better comparison with the UV (u') surface brightness distribution for supernova environments, as reported by Kelly & Kirshner (2012) than made by Chrimes et al. (2024) with F555W. The Galactic extinction-corrected F336W surface brightness is in the faintest ∼10% for local supernova values; this is therefore faint but not unprecedented.

3.2. Global host properties

We next consider how the overall host galaxy properties compare with the local environment of AT 2023fhn, and how they compare with the hosts of other LFBOTs. To do this, we perform spectral energy distribution (SED) fitting of the integrated light of the host. By host, we refer to the spiral and satellite galaxy together, since their proximity likely results in interactions (e.g. tidal) and therefore the two galaxies can be considered as one interacting system. Furthermore, the two galaxies are not spatially resolved in ground-based imaging (e.g. PanSTARRS), which we used to add photometric points to the SED.

We attempt to collect as close to 100% of the galaxy light from HST photometry as possible. We measure the Petrosian radius $R_{\rm petro}$ (Petrosian 1976) of the spiral galaxy with the STATMORPH package (Rodriguez-Gomez et al. 2019, η = 0.2) and adopt 1.5 $R_{\rm petro}$ as a radius that encloses ∼100% of the flux (e.g. Conselice 2003). We account for the projected ellipticity and orientation of the galaxy using the ELLIP and THETA outputs. A pixel mask is produced using these parameters as measured from the F555W image, and applied to the other HST images, as shown in Fig. 2. The flux within the mask is summed, and background subtraction (as for the local environment measurements above) uses the sigma-clipped median background, scaled for the number of pixels in the mask. Repeating the procedure for the satellite galaxy produces a 1.5 $R_{\rm petro}$ pixel mask that lies entirely within the spiral's mask. We therefore use spiral pixel mask alone as it captures ∼100% of the flux from both galaxies. Uncertainties are determined using the standard deviation of background pixels outside the galaxy mask, again using background estimator, the total background noise on the measurement is then $\sqrt{N}\times\sigma_{bg}$. To investigate the effect of background variations, we split each image into regions of 400 × 400 pixels – the approximate size of the galaxy mask – and determine the median background level in each region. The standard deviation of these, that is, the uncertainty in the background level, is added in quadrature as an additional source of error on our HST galaxy photometry.

To supplement the HST data we add host photometry from archival catalogues. For additional optical points we use PanSTARRS data release 2 (Chambers et al. 2016). We use the catalogued Kron magnitudes (Kron 1980, in g, r, i, z and y), which capture ∼90% of the light of extended sources, and increase the fluxes by a further 10% to approximate the ∼100% flux value[3]. The Kron radii for the spiral (4.41, 4.62, 4.36, 3.33 and 2.89 arcsec in g, r, i, z, y respectively) extend past the position of the satellite in g, r, i, so the system can be considered blended in these filters. In y and z this is not the case, so they likely underestimate the flux from the combined galaxy-satellite system, and indeed these points lie a few sigma below the best-fit spectrum when they are included in the fit. We therefore remove the y and z filters from the fitting. We also add far-UV and near-UV photometry from GALEX (Martin et al. 2003), plus W1, W2

[3] https://outerspace.stsci.edu/display/PANSTARRS/PS1+Kron+photometry+of+extended+sources

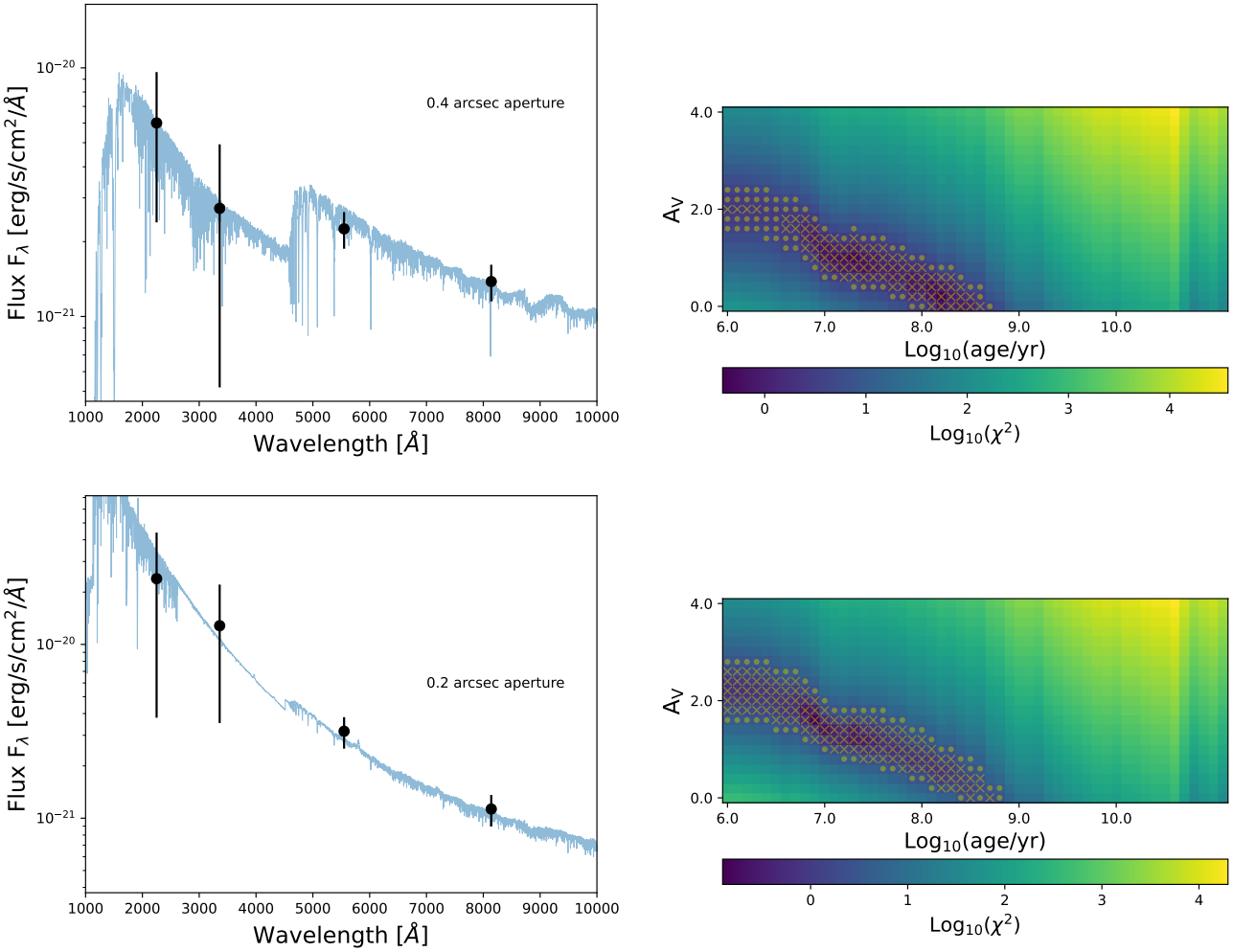

Fig. 3. Epoch 2 HST photometry at the location of AT 2023fhn, corrected for Galactic extinction, and fit to BPASS single age spectral models while allowing the (intrinsic) extinction to vary. Top row, left: the best fit single-age BPASS spectrum. Wavelengths are observer frame. The photometry was measured with median background subtraction and a 0.4 arcsec aperture, and is corrected for both Galactic and instrinsic extinction. Top row, right: the colourmap corresponds to the fit $\log_{10}(\chi^2)$ as a function of intrinsic extinction and age. We find a best fitting combination of $\mathrm{Log(age/yr)} = 8.2^{+0.4}_{-2.2}$ and $\mathrm{A_V} = 0.2^{+1.8}_{-0.2}$ (uncertainties at 68% confidence, Avni 1976). Pixels in the parameter space grid within the 68% and 90% confidence regions are indicated by crosses (within 68%) and dots (in the 68–90% range). Bottom row: as for the upper row, but using a 0.2 arcsec aperture for photometry, with which we find $\mathrm{Log(age/yr)} = 6.9^{+1.8}_{-0.9}$ and $\mathrm{A_V} = 1.6^{+1.0}_{-1.6}$.

and W3 detections from WISE. Effective wavelengths for these filters are taken from Tonry et al. (2012). The spiral and satellite cannot be separated at the spatial resolution of these surveys, and neither galaxy is detected in 2MASS. The full list of photometry used to performed SED fitting is provided in Table 1.

To perform SED fitting we use PROSPECTOR (Leja et al. 2017; Johnson et al. 2021), which makes use of FSPS (Flexible Stellar Population Synthesis Conroy et al. 2009; Conroy & Gunn 2010) and Python-FSPS (Johnson et al. 2023). For the Markov Chain Monte Carlo (MCMC) implementation we use EMCEE (Foreman-Mackey et al. 2013). We again use BPASS (Binary Population and Spectral Synthesis v2.1, Eldridge et al. 2017; Stanway & Eldridge 2018) for the spectral models. Before being passed to PROSPECTOR, the input photometry is corrected for Galactic extinction (as described in Sect. 3.1). We fit four parameters: the stellar mass $M_\star$, intrinsic (local to the transient) extinction A_V, population age t_age and the timescale for an exponentially declining star-formation history τ. The redshift is fixed at $z = 0.238$, and the luminosity distance at $D_\mathrm{L} = 1192$ Mpc.

We run the MCMC with 128 walkers and 512 iterations; the full list of MCMC set-up parameters and joint posterior distributions (in the form of a corner plot) are provided in Appendix B. The maximum a posterior (MAP) spectrum is shown in Fig. 4, with the associated properties from the posterior distribution listed in Table 2. Thus far, the metallicity Z has been fixed at half-Solar, based on the approximate mass of 10^{10} M$_\odot$ and the mass-metallicity relation (Tremonti et al. 2004; Gallazzi et al. 2005). A similar table containing the results when metallicity is allowed to vary is also provided in Appendix B. In this case, the mass and SFR are similar, such that fixing Z at a more realistic value does not change our results in a qualitative sense. In the delayed-τ model, the current star-formation rate (SFR) is proportional to $(t/\tau)e^{(-t/\tau)}$. The absolute value is obtained by normalisation with respect to the mass formed, yielding a SFR of 5.5 M$_\odot$ yr^{-1}. In Fig. 4, the F845M point lies above the best fit spectrum, possibly due to the presence of Hα emission in this medium-width filter. Using the offset between the F845M point and the best-fit spectrum, and assuming the offset is dominated by Hα emission, we estimate the line flux as $\sim 1\times10^{-19}$ erg s^{-1} cm^{-2} Å^{-1}, which

Table 1. Host galaxy photometry used for SED fitting.

Filter	Source	m	err	$\lambda_{\rm eff}$ [Å]	A(λ)
FUV	GALEX	20.93	0.31	1548.85	0.20
NUV	GALEX	20.74	0.25	2303.37	0.22
F225W	HST	20.60	0.07	2358.70	0.20
F336W	HST	20.40	0.03	3359.11	0.13
g	PS	19.70	0.01	4810.00	0.09
F555W	HST	19.34	0.01	5235.33	0.08
r	PS	19.17	0.01	6170.00	0.07
i	PS	18.93	0.01	7520.00	0.05
F763M	HST	18.93	0.01	7602.85	0.05
F814W	HST	18.84	0.01	7954.84	0.04
F845M	HST	18.68	0.02	8430.20	0.04
W1	WISE	18.91	0.07	33 526.00	0.00
W2	WISE	18.82	0.13	46 028.00	0.00
W3	WISE	16.92	0.38	115 608.00	0.00

Notes. All magnitudes are in the AB system, and before Galactic extinction correction. The filter effective wavelengths and Galactic extinction at that wavelength – assuming $E(B-V) = 0.0254$, $R_V = 3.1$ and a Fitzpatrick (1999) extinction law – are also listed. We increase the PanSTARRS fluxes by 10% over the values below, as described in the text.

corresponds to a SFR of $\sim 1\,M_\odot\,yr^{-1}$ (Kennicutt et al. 1994). However, since the F845M point is only offset by $\sim 3\sigma$, and given the uncertainty in the continuum level, we use continue to use the PROSPECTOR derived SFR as the fiducial value.

In summary, the galaxy pair is dominated by a fairly typical star-forming spiral, but is perhaps notable for the likely presence of tidal interactions between the spiral and its satellite. In Fig. 5 we plot its mass versus SFR, comparing with the host galaxies of previous LFBOTs. The galaxy has a high SFR and mass for LFBOT hosts, lying slightly above average in terms of specific star formation rate (sSFR), but well below the sSFR of the host of ZTF 18abvkwla.

4. Transient emission

4.1. UV-optical

We now compare the UV-optical constraints on AT 2023fhn's light curve with previous LFBOTs. All times used in Sect. 4 are in the rest-frames of the LFBOTs. Comparison data are corrected for Galactic extinction of $E(B-V) = 0.08$ (AT 2018cow, Prentice et al. 2018) and $E(B-V) = 0.07$ (ZTF 20acigmel, Perley et al. 2021), their UV light curves (in absolute magnitude) are compared with AT 2023fhn in Fig. 6. We fit the light curve of AT 2018cow in 2 phases, early (<200 d) and late-time, with a fit of the form $M = a\log(t)^b + c$. For the fit to AT 2018cow, we assume that the late-time UV is dominated by residual transient emission (Sun et al. 2022, 2023; Chen et al. 2023; Inkenhaag et al. 2023). We shift the AT 2018cow best-fit up in absolute magnitude such that it lies between the early-time ATLAS *c*-band and FORS2 *u*-band AT 2023fhn detections (Ho et al. 2023c). The extrapolated curve passes below the late-time HST F225W and F336W upper limits reported in this work. Another LFBOT with good UV photometric coverage is ZTF 20acigmel, but here we consider only the early, pre-break phase due to a lack of late-time constraints. ZTF 20acigmel starts brighter than AT 2018cow and fades faster, whereas AT 2023fhn is the most luminous LFBOT yet at UV-optical wavelengths.

A final addition to Fig. 6 are bands of constant UV absolute magnitude, corresponding to late-time emission from black holes of different masses in the tidal disruption event model of Mummery et al. (2024). This model yielded a black hole mass of $\sim 10^3\,M_\odot$ for AT 2018cow. Assuming that AT 2023fhn had a similar light-curve shape to AT 2018cow – which may not be the case for accretion events around black holes of different masses – the HST F336W point source upper limit for AT 2023fhn tentatively constrains the accreting black hole mass in a TDE interpretation to $\lesssim 10^5\,M_\odot$.

4.2. X-ray

Figure 7 shows our X-ray observations of AT 2023fhn, and the X-ray light curves of other LFBOTs. The AT 2018cow broken power-law and late-time plateau fit of Migliori et al. (2024) is also shown. AT 2023fhn is the faintest LFBOT in X-rays at early times. Assuming a shallow decay initially, similar to AT 2022tsd, ZTF 20acigmel and AT 2018cow, the break time can be – at the latest – similar to AT 2018cow and ZTF 20acigmel. Notwithstanding the small sample size, among the three LFBOTs with a clearly observed break in the X-ray light curve (AT2018 cow, ZTF20 acigmel and AT 2022tsd), brighter LFBOTs seem to transition to a steeper decay at later times. Assuming instead that epochs 1 and 2 are on the same phase of the light curve, the decay index $n = 2.1^{+0.7}_{-0.9}$ (where $L \propto t^{-n}$). Expectations for the X-ray decay rate are t^{-1} (shock power), t^{-2} (magnetar central engine) and $t^{-5/3}$ (fallback, i.e. a TDE). Overall, the detections and upper-limits are consistent with AT 2023fhn behaving like a fainter version of previous LFBOTs in the X-ray band, and demonstrates that they can exhibit several orders of magnitude of variety in their X-ray luminosity.

4.3. UV/X-ray ratio

Motivated by the fact that AT 2023fhn appears to be the brightest LFBOT yet at UV-optical wavelengths, and the faintest in terms of X-ray luminosity, in Fig. 8 we show the ratio of X-ray to UV luminosity for the 3 LFBOTs with such constraints. The data points for AT 2023fhn take the X-ray detections at 12 and 23 rest-frame days, and the corresponding point on the shifted AT 2018cow light curve in Fig. 6. The uncertainties shown are exclusively from the X-ray observations. For AT 2018cow, we take the ratio of the X-ray fit of Migliori et al. (2024) in Fig. 7, and our fit to the UV light-curve fit in Fig. 6. Finally, for ZTF 20acigmel we take the ratio of the X-ray luminosity with the UV light-curve fit at the same time. LFBOTs therefore exhibit at least ~3 orders of magnitude in their X-ray/UV luminosity ratio, even at similar times in their evolution. This is plausibly a viewing angle effect. A qualitative prediction of tidal disruption models is a trade-off between UV-optical and X-ray luminosity as a function of viewing angle, where on-axis angles (which may also be aligned with a beamed outflow) would see a higher X-ray luminosity (Dai et al. 2018; Hayasaki & Jonker 2021). Differences in L_X/L_{UV} are also expected for different black hole masses and spins, due to varying accretion disc formation rates (which in turn affects the delay betweeen peak X-ray and UV/optical emission, Jonker et al. 2020). However, a scenario in which the peak X-ray emission is delayed due to a delay in forming the inner accretion disc is hard to reconcile with the energetics and (variability) timescales of LFBOT emission, which demands energy input from a central engine and therefore active accretion (e.g. Ho et al. 2019; Margutti et al. 2019). Alternatively, the range of L_x/L_{UV} could reflect differences in the circumstellar media, which we investigate in the following section.

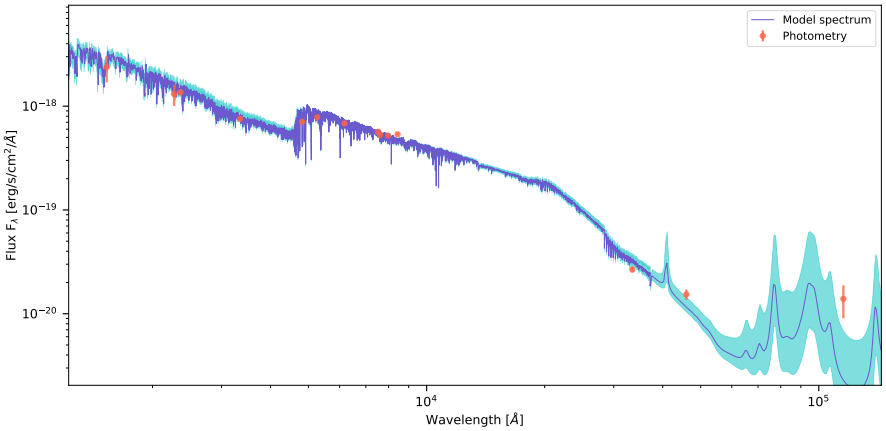

Fig. 4. Host galaxy photometry and best-fit spectrum from PROSPECTOR. The model spectrum is red-shifted into the observer frame. A light blue shaded region encloses the 90% confidence interval on the posterior flux distribution at each wavelength. The photometry is from GALEX, PanSTARRS, WISE and HST/WFC3 as listed in Table 1, and is corrected for Galactic extinction with the Python module EXTINCTION at the filter effective wavelengths. The corresponding galaxy properties are listed in Table 2.

Table 2. Host galaxy properties derived from PROSPECTOR SED fitting.

Host property	Value
$M_\star/M_\odot$	$(1.29^{+0.08}_{-0.07}) \times 10^{10}$
SFR/$M_\odot$ yr^{-1}	$5.5^{+1.1}_{-0.7}$
A_V	0.20 ± 0.07
t_{age}/Gyr	$1.68^{+0.29}_{-0.20}$
τ/Gyr	$0.66^{+0.31}_{-0.13}$

Notes. The median values from the marginalised posterior distributions are quoted, with uncertainties bounding the 68% confidence interval on each parameter.

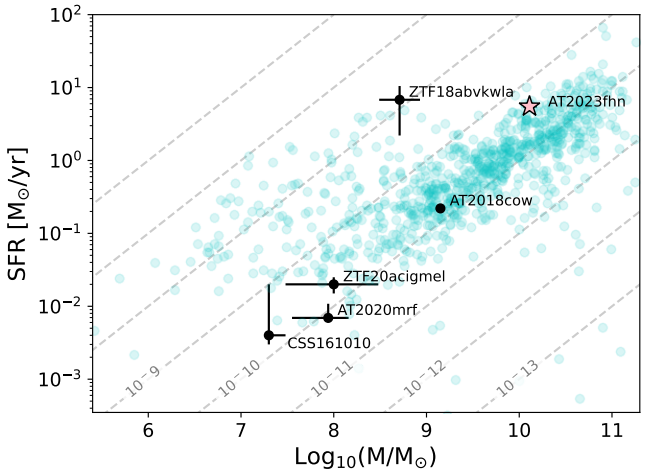

Fig. 5. Stellar mass versus SFR for LFBOT host galaxies, including AT 2023fhn. Other LFBOT host data are from Perley et al. (2019, AT 2018cow), Ho et al. (2020, ZTF 18abvkwla), Coppejans et al. (2020, CSS161010) and Perley et al. (2021, ZTF 20acigmel). Lines of constant specific star formation rate (sSFR/yr^{-1}) are drawn in grey. The core-collapse supernova host galaxy sample of Schulze et al. (2021) is plotted as transparent cyan points.

4.4. Radio

Assuming that the radio emission is synchrotron-dominated with self-absorption – as we will see, the radio SED of AT 2023fhn is consistent with this – and that the peak of the SED occurs at the synchtrotron self-absorption (SSA) frequency, we can estimate several shock parameters, and properties of the circumstellar medium. We follow the synchrotron self-absorption model

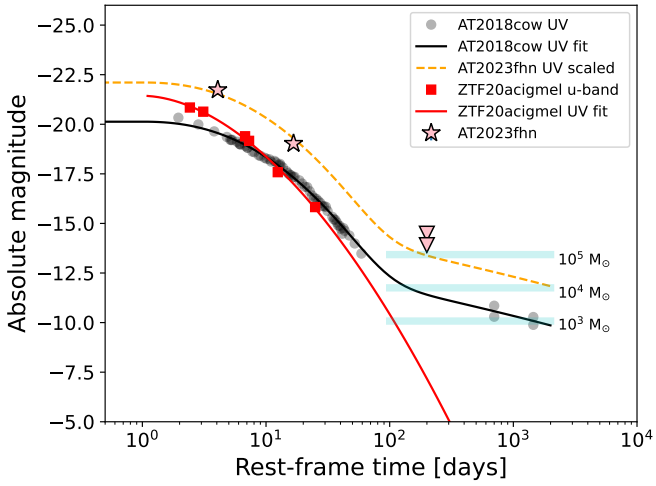

Fig. 6. UV data points for AT 2023fhn, compared with the UV light curves of AT 2018cow (Early u-band and late-time F222W and F336W, Prentice et al. 2018; Perley et al. 2019; Inkenhaag et al. 2023) and ZTF 20acigmel (Perley et al. 2021). A light-curve fit to the AT 2018cow data is increased in luminosity to intercept the sole early-time AT 2023fhn UV point, the subsequent F336W limit at ∼112 rest-frame days lies just above the expected UV magnitude at this epoch, assuming identical evolution to the Cow. A similar fit is made for the early-time ZTF 20acigmel points. Cyan horizontal bands show the expected UV absolute magnitudes at late times for accretion discs around IMBHs of different masses, following a tidal disruption event (Mummery et al. 2024).

of Chevalier (1998) (see also Soderberg et al. 2005). Adopting this framework for AT 2023fhn is reasonable since this best fits other LFBOTs studied so far (based on the brightness temperature, which precludes thermal emission, and the spectral shape, e.g. Margutti et al. 2019; Coppejans et al. 2020; Ho et al. 2020, 2022; Nayana & Chandra 2021; Yao et al. 2022; Bright et al. 2022).

We fit the radio spectrum at ∼90 and ∼138 days (∼70 and ∼110 rest-frame days) following Chevalier (1998), Granot & Sari (2002), Chevalier & Fransson (2006). At a given time t the radio SED has the form,

$$F(\nu) = F_{\rm pk}\left[\left(\frac{\nu}{\nu_{\rm pk}}\right)^{-s\beta_1} + \left(\frac{\nu}{\nu_{\rm pk}}\right)^{-s\beta_2}\right]^{-\frac{1}{s}}, \quad (1)$$

where $F(\nu)$ is the flux density, $F_{\rm pk}$ is the flux at the peak (break) frequency $\nu_{\rm pk}$ where the optically thick and thin power laws

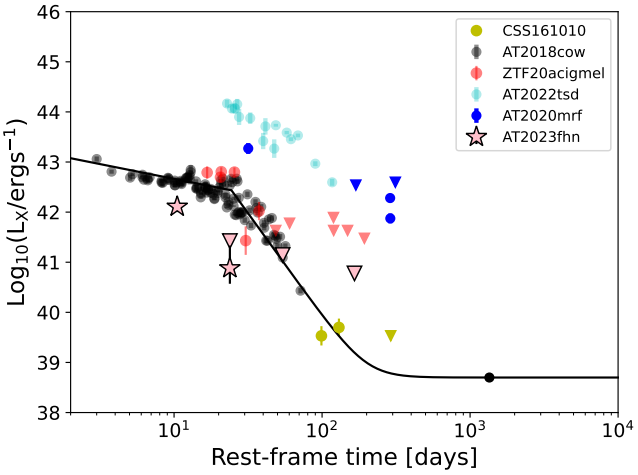

Fig. 7. X-ray light curve of AT 2023fhn compared with other LFBOTs. All data are in the ~0.5–10 keV range, are unabsorbed and from Rivera Sandoval et al. (2018; 2019; 2024, AT 2018cow), Coppejans et al. (2020, CSS161010), Bright et al. (2022; 2022, ZTF 20acigmel), Yao et al. (2022, AT 2020mrf) and Matthews et al. (2023, AT 2022tsd). Given the marginal nature of the second AT 2023fhn measurement, we also plot the 2σ upper limit at this epoch. A broken-power law and late-time plateau interpretation of AT 2018cow's light curve is shown by the solid black line (Migliori et al. 2024).

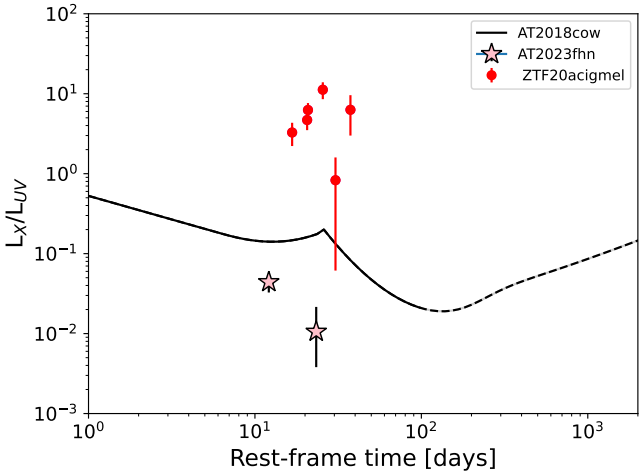

Fig. 8. Ratio of X-ray to UV luminosity for LFBOTs AT 2023fhn, AT 2018cow, and ZTF 20acigmel. The AT 2023fhn points use the dashed orange line in Fig. 6 and the two *Chandra* X-ray detections (errorbars reflect the X-ray uncertainties only). The black curve is the ratio of the Migliori et al. (2024) X-ray light-curve fit (see the solid black line, Fig. 7) and a broken power-law fit to the UV observations (the solid black line in Fig. 6). The small k-corrections are neglected in this comparison. The evolution past 200 days (drawn as a dashed line) is highly uncertain due to the sole X-ray detection. The ZTFacigmel data are from Ho et al. (2022), Bright et al. (2022), where we have taken the ratio of X-ray points and the power-law fit to the ZTFacigmel UV light curve in Fig. 6. The uncertainties on these points again solely reflect the X-ray measurement uncertainties.

intersect, s is a smoothing factor and β_1 and β_2 are spectral indices in the optically thick and thin regimes, respectively. In our case the cooling frequency ν_c lies at higher frequencies than probed by our observations (~400–800 GHz), where ν_c is given by $18\pi m_e ce)/(t^2\sigma_t^2 B^3)$ (DeMarchi et al. 2022). We therefore expect $F(\nu) \propto \nu^{-(p-1)/2}$ in the optically thin regime, where p is the power law index of the electron energy distribution in the shock (i.e. the number N of electrons with Lorentz factor γ_e goes as $N(\gamma_e) \propto \gamma_e^{-p}$).

Using the SCIPY CURVE_FIT function, and working with rest-frame times and central frequencies throughout this section, we fit Eq. (1) to the ~90 day and ~138 day (observer frame) data. At 90 days we have 6 data points (5 detections, 1 upper limit, we combine the 87 and 95 day data for this epoch), and at 138 days we have 7 data points (6 detections, 1 upper limit). The data points (including limits, which use the RMS as σ) are given a $1/\sigma^2$ weighting (with SIGMA_ABSOLUTE = FALSE). There are 5 parameters to fit: $F_{\rm pk}$, $\nu_{\rm pk}$, β_1, β_2 and s. The best-fit values for these parameters and their uncertainties (calculated from the covariance matrix output by CURVE_FIT) are listed in Table 3. The optically thin spectral index of –0.6 (138 days) yields an electron energy spectral index of ~2.2, which is relatively shallow; 2.5 is expected from theory, while values closer to ~3 are often measured in gamma-ray bursts, tidal disruption events and supernovae (e.g. Chevalier & Fransson 2006; Cendes et al. 2024). Values from other LFBOTs are also in the range ~2–3 (Margutti et al. 2019; Ho et al. 2020; Coppejans et al. 2020; Yao et al. 2022; Bright et al. 2022).

The peak flux $F_{\rm pk}$ and (rest-frame) frequency at the peak flux $\nu_{\rm pk}$ (at the intersection of the power-laws, rather than the fitted peak) allow us to estimate the radius of the shock, circumstellar density at that radius, and the CSM surface density parameter $A_\star \propto \dot{M}/v_w$ (see DeMarchi et al. 2022, for a detailed description of the modelling assumptions). Following the formulism of Chevalier (1998) (see also Chevalier & Fransson 2006; DeMarchi et al. 2022; Bright et al. 2022), we first have the shock radius $R_{\rm p}$, given by,

$$R_{\rm p} = 4\times10^{14}\left(\frac{\epsilon_{\rm e}}{\epsilon_{\rm B}}\right)^{\frac{-1}{19}}\left(\frac{f}{0.5}\right)^{\frac{-1}{19}} \left(\frac{F_{\rm pk}}{(1+z)\,{\rm mJy}}\right)^{\frac{9}{19}}\left(\frac{D_\theta}{\rm Mpc}\right)^{\frac{18}{19}}\left(\frac{\nu_{\rm pk}}{5\,{\rm GHz}}\right)^{-1}{\rm cm}, \quad (2)$$

where D_θ is the angular diameter distance, and ϵ_e and ϵ_B are the fraction of the shock energy in electrons and in the magnetic field, respectively. The average shock velocity can then be calculated as $R_{\rm p}/t_{\rm obs} = \Gamma\beta c$, where $\beta = v/c$, Γ is the Lorentz factor and $t_{\rm obs}$ is the rest-frame observation time. Next we have, for the internal magnetic field B,

$$B = 1.1\left(\frac{\epsilon_{\rm e}}{\epsilon_{\rm B}}\right)^{\frac{-4}{19}}\left(\frac{f}{0.5}\right)^{\frac{-4}{19}}\left(\frac{F_{\rm pk}}{(1+z)\,{\rm mJy}}\right)^{\frac{-2}{19}}\left(\frac{D_\theta}{\rm Mpc}\right)^{\frac{-4}{19}}\left(\frac{\nu_{\rm pk}}{5\,{\rm GHz}}\right){\rm G} \quad (3)$$

and for the wind density (the mass loss rate $\dot{M}$ over the wind velocity),

$$\frac{\dot{M}}{v_{\rm w}}\left(\frac{1000\,{\rm km\,s^{-1}}}{10^{-4}\,{\rm M_\odot\,yr^{-1}}}\right) = 2.5\times10^{-5}\left(\frac{1}{\epsilon_{\rm B}}\right)\left(\frac{\epsilon_{\rm e}}{\epsilon_{\rm B}}\right)^{\frac{-8}{19}}\left(\frac{f}{0.5}\right)^{\frac{-8}{19}}\times \left(\frac{F_{\rm pk}}{(1+z)\,{\rm Jy}}\right)^{\frac{-4}{19}}\left(\frac{D_\theta}{\rm Mpc}\right)^{\frac{-8}{19}}\left(\frac{\nu_{\rm pk}}{5\,{\rm GHz}}\right)^2\left(\frac{t_{\rm pk}}{\rm days}\right)^2. \quad (4)$$

Under the assumption that the CSM is dominated by fully ionised hydrogen, the electron number density can be related to $\dot{M}/v_w$ by $n_e = \dot{M}/(4\pi m_p r^2 v_w)$ – where m_p is the proton mass – so that

$$n_{\rm e} = 1.02418\left(\frac{1}{\epsilon_{\rm B}}\right)\left(\frac{\epsilon_{\rm e}}{\epsilon_{\rm B}}\right)^{\frac{-6}{19}}\left(\frac{f}{0.5}\right)^{\frac{-6}{19}}\times \left(\frac{F_{\rm pk}}{(1+z)\,{\rm Jy}}\right)^{\frac{-22}{19}}\left(\frac{D_\theta}{\rm Mpc}\right)^{\frac{-44}{19}}\left(\frac{\nu_{\rm pk}}{5\,{\rm GHz}}\right)^4\left(\frac{t_{\rm pk}}{\rm days}\right)^2 {\rm cm^{-3}}. \quad (5)$$

Table 3. Radio SED fit results using the ~90 day data, left, and ~138 day data, right, with Eq. (1).

$t \sim 90$ days		
Parameter	Unit	Value
$\nu_{\rm pk}$	GHz	3.6 ± 0.2
$L_{\nu,\rm pk}$	erg s^{-1} Hz^{-1}	$(3.6 \pm 0.3) \times 10^{29}$
β_1	–	4 ± 1
β_2	–	-0.6 ± 0.1
$R_{\rm p}$	10^{17} cm	1.3 ± 0.1
$v/c = \Gamma\beta$	–	0.72 ± 0.03
$\dot{M}/v_w$	10^{-4} M$_\odot$ yr^{-1} / 1000 km s^{-1}	0.08±0.01
n_e	cm^{-3}	20 ± 2
B	G	0.24±0.02
U	10^{49} erg	$2.2^{+0.3}_{-0.2}$
$R_{\rm p}$	10^{17} cm	1.2 ± 0.1
$v/c = \Gamma\beta$	–	0.63 ± 0.03
$\dot{M}/v_w$	10^{-4} M$_\odot$ yr^{-1} / 1000 km s^{-1}	0.94±0.02
n_e	cm^{-3}	$(3.2^{+0.4}_{-0.3})\times10^2$
B	G	0.15±0.01
U	10^{49} erg	19 ± 2
$t \sim 138$ days		
Parameter	Unit	Value
$\nu_{\rm pk}$	GHz	5.0 ± 0.7
$L_{\nu,\rm pk}$	erg s^{-1} Hz^{-1}	$(6.0 \pm 0.9) \times 10^{29}$
β_1	–	2.8 ± 0.8
β_2	–	-0.6 ± 0.2
$R_{\rm p}$	10^{17} cm	1.2 ± 0.1
$v/c = \Gamma\beta$	–	0.42 ± 0.03
$\dot{M}/v_w$	10^{-4} M$_\odot$ yr^{-1} / 1000 km s^{-1}	0.32 ± 0.01
n_e	cm^{-3}	$(1.0 \pm 0.2) \times 10^2$
B	G	0.31 ± 0.01
U	10^{49} erg	2.9 ± 0.5
$R_{\rm p}$	10^{17} cm	1.1 ± 0.1
$v/c = \Gamma\beta$	–	0.37 ± 0.03
$\dot{M}/v_w$	10^{-4} M$_\odot$ yr^{-1} / 1000 km s^{-1}	4.0 ± 0.1
n_e	cm^{-3}	$(1.6^{+0.3}_{-0.2}) \times 10^3$
B	G	0.19 ± 0.03
U	10^{49} erg	25^{+5}_{-4}

Notes. Above the single solid lines we list the broken power-law fit parameters. Below, we list the inferred event properties at each epoch under the synchrotron blast-wave model as described in Sect. 4.4, assuming equipartition ($\epsilon_e = \epsilon_B = 1/3$). The uncertainties on the event properties (provided at 1σ) are statistical only, and are underestimated due to the presence of systematic errors arising from fixed values of f, $\epsilon_{\rm e}$ and $\epsilon_{\rm B}$. We also allowed s to vary between 0 and 1, with $s = 1$ providing the best-fit in each case. The (rest-frame) fit parameters $\nu_{\rm pk}$ and $L_{\nu,\rm pk}$ are defined at the intersection point of the two power laws (Chevalier 1998). Below the double lines we give parameter values calculated with $\epsilon_e = 0.1$ and $\epsilon_B = 0.01$ (note that only the results with $\epsilon_e = \epsilon_B = 1/3$ are plotted in the relevant figures).

Additionally we have, for the internal shock energy $U = U_{\rm B}/\epsilon_{\rm B}$,

$$U = 1.859 \times 10^{46} \left(\frac{1}{\epsilon_{\rm B}}\right)\left(\frac{\epsilon_{\rm e}}{\epsilon_{\rm B}}\right)^{\frac{-11}{19}}\left(\frac{f}{0.5}\right)^{\frac{8}{19}} \times \left(\frac{F_{\rm pk}}{(1+{\rm z})\,{\rm Jy}}\right)^{\frac{23}{19}}\left(\frac{D_\theta}{\rm Mpc}\right)^{\frac{46}{19}}\left(\frac{\nu_{\rm pk}}{5\,{\rm GHz}}\right)^{-1} {\rm erg}. \quad (6)$$

We assume equipartition ($\epsilon_e = \epsilon_B = 1/3$), where the magnetic energy density, the energy density in electrons and the energy density in protons contribute equally as destinations for the converted kinetic energy in the shock. We further assume $f = 0.5$ for the filling factor. If the emission region is modelled as a disc of radius R and thickness S on the sky, whose volume is $\pi R^2 S$, an equivalent spherical volume can be given by $4/3\pi R^3$. The filling factor is the fraction of this equivalent spherical volume producing emission (Chevalier 1998).

We list the inferred properties of AT 2023fhn's blast wave in Table 3. Results for the fiducial parameters of $\epsilon_e = 0.1$ and $\epsilon_B = 0.01$ are also listed. These properties are compared with other LFBOTs in Figs. 9, 10, and 11. In LFBOTs the expanding blast wave typically shows a SSA spectrum that decreases in peak flux and frequency over time. However we note that AT2023fhn shows an increase in peak flux between ~90 and ~138 days post explosion. A similar increase was seen in CSS161010 between 69 and 99 days post explosion (Coppejans et al. 2020). This could potentially be caused by an increase in density, or inhomogeneities in the CSM, but we are not able to test this scenario given our weak constraints on the SSA peak at ~90 days post explosion.

Finally, we calculate a dimensionless normalisation of the wind density parameter $A_\star \propto n_e r^2 \propto \dot{M}/v_w$ (Chevalier & Li 2000),

$$A_\star = \frac{\dot{M}}{(5 \times 10^{11}\,{\rm g\,cm^{-1}}) \times 4\pi v_w} \quad (7)$$

where $A_\star = 1$ for a Wolf-Rayet-like wind with $\dot{M} = 10^{-5}\,{\rm M_\odot\,yr^{-1}}$ and $v_w = 1000\,{\rm km\,s^{-1}}$. From our best fits to the radio data, we derive that AT 2023fhn at ~70–110 rest-frame days has $A_\star \sim 1$ (~0.1×10^{-4} M$_\odot$ yr^{-1} for $v_{\rm w} = 1000$ km s^{-1}). This mass loss rate is consistent with that of Wolf-Rayet stars. As shown in Fig. 11, this density is also consistent with that of the other LFBOTs. The constraints on the synchrotron self-absorption peak at ~90 days post explosion were unfortunately insufficient to constrain the density profile of the CSM around AT 2023fhn.

5. Discussion

In this section we discuss the host galaxy and derived properties of AT 2023fhn in the context of the other LFBOTs discovered thus far. The host of AT 2023fhn, taking the spiral and satellite as one interacting system, is broadly consistent with the host galaxies of core-collapse supernovae, and slightly above four other LFBOT hosts in terms of specific star formation rate (although below the host of ZTF 18abvkwla). The host offset and faint, diffuse emission at the transient location (see Sect. 3.1) are consistent with the tail of the core-collapse supernova distribution (see also Chrimes et al. 2024). While the local and broader environment is consistent with a core-collapse origin, it is interesting to consider whether the high sSFR is related to tidal interaction between the spiral and satellite galaxy. Such interactions may be associated with an elevated tidal disrupted event (TDE) rate, which show a bias towards occurrence in the nuclei of post-starburst galaxies and galaxies undergoing interactions/mergers (French et al. 2016). The non-nuclear location of AT 2023fhn – at high offset from both the spiral and satellite – is difficult to explain in such a scenario (Chrimes et al. 2024), since galaxy-galaxy interactions are unlikely to have much impact on the TDE rate in massive clusters well away from the nuclei of either galaxy. On the other hand, galaxy scale interactions

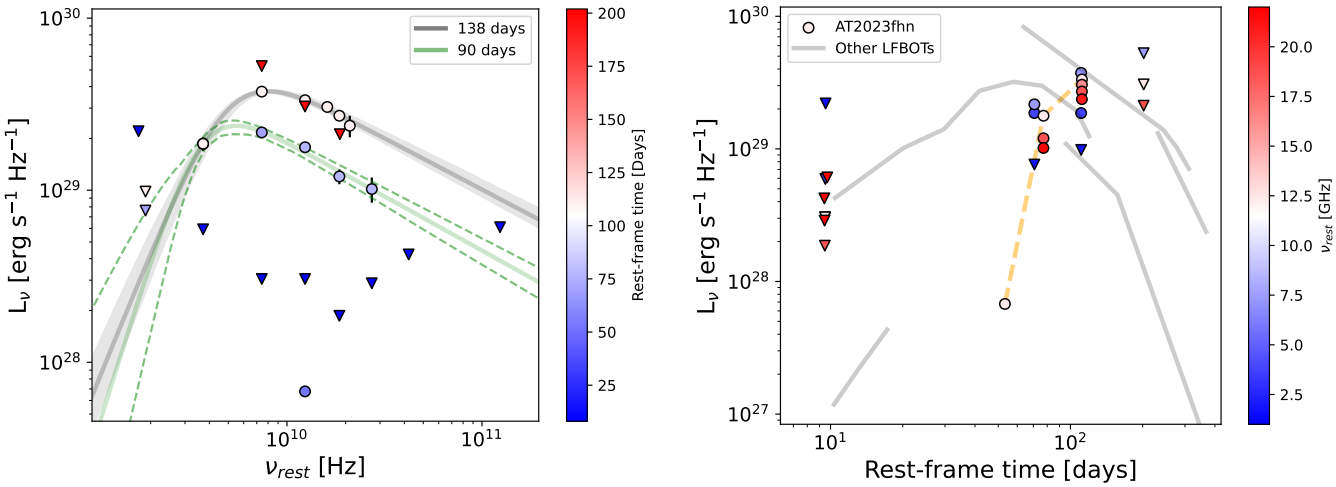

Fig. 9. Radio observations of AT 2023fhn (see Table A.3) placed in the context of other LFBOTs. Upper limits from NOEMA and the VLA as reported by Ho et al. (2023d) and Ho (2023) are also shown. Left: radio SED for AT 2023fhn, with a broken-power law fit to the $t = 138$ day (grey line) and $t = 90$ day (green line) data. Data point rest-frame times are indicated by the colourbar. The 90% confidence regions on the fits are shown by light grey shading (138 days) and dashed green lines (90 days). It is important to note that there are overlapping data points at ∼3 Ghz (i.e. a 90 day point with similar luminosity is obscured by the 138 day point). Right: radio light curve for AT 2023fhn (central frequencies indicated by the colourbar) and other LFBOTs. The 10 GHz AT 2023fhn detections are connected by a dashed orange line, to aid the eye in comparing with other LFBOTs. Data for the other LFBOTs, all at (10 ± 2) GHz, are from Ho et al. (2019; 2019, AT 2018cow), Ho et al. (2020, ZTF 18abvkwla), Coppejans et al. (2020, CSS161010), Bright et al. (2022), Ho et al. (2022, ZTF 20 acigmel) and Yao et al. (2022, AT 2020mrf).

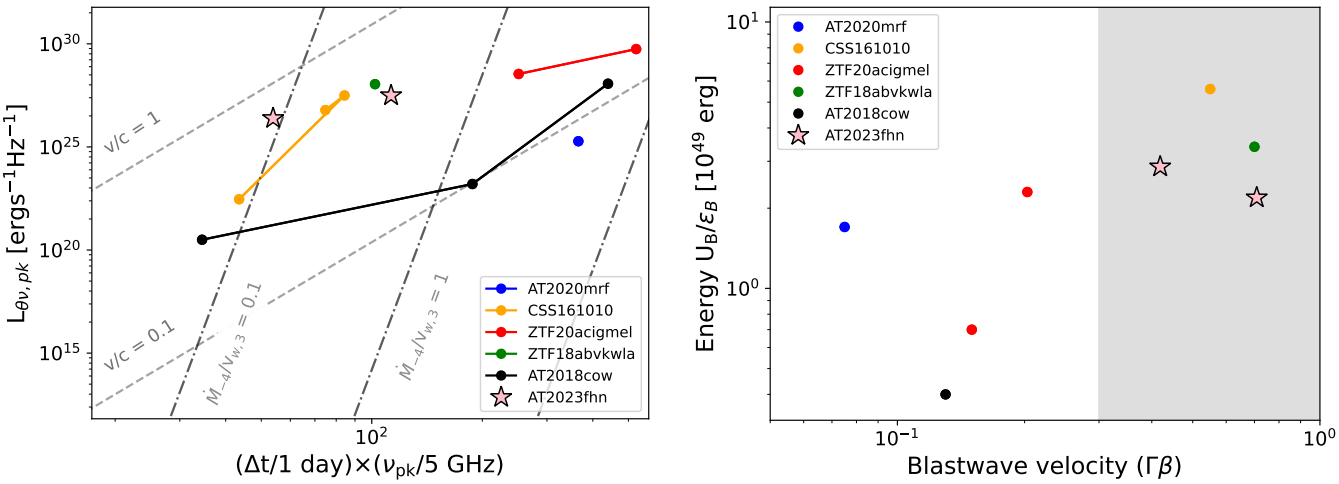

Fig. 10. Results from fitting a synchrotron blast wave model to AT2023fhn. Left: the product of rest-time Δt and the rest-frame peak frequency $\nu_{\rm pk}$ at that time, versus the peak radio spectral luminosity $L_{\theta\nu,\rm pk} = L_{\nu,\rm pk}/(1+z)^3$, with lines of constant $\dot{M}/V_w$ (in units of 10^{-4} M$_\odot$ yr^{-1}/1000 km s^{-1}) and lower limits on the blast-wave velocity shown. Both AT 2023fhn epochs are shown, we note that constraints on the later point (138 days) are stronger and the parameters at this epoch better constrained. All comparison data points adopt $\epsilon_e = \epsilon_B = 1/3$. Right: lower limits on the average blast-wave velocity (blast-wave radius over the rest-frame time) in units of c versus the internal energy of the shock $U = U_B/\epsilon_B$. Other LFBOT data are taken from Ho et al. (2019; 2019; 2021, AT 2018cow), Ho et al. (2020, ZTF 18abvkwla), Coppejans et al. (2020, CSS161010), Bright et al. (2022), Ho et al. (2022, ZTF 20 acigmel) and Yao et al. (2022, AT 2020mrf). The mildly relativistic regime is shaded. We have scaled the Bright et al. (2022) ZTF 20 acigmel point following Eqs. (2) and (6) to align with our assumption of equipartition.

may increase the chance of finding a massive (possibly IMBH-hosting, Fragione et al. 2018) cluster in such a location (e.g. Napolitano et al. 2022), even if they do not increase the TDE rate within the cluster.

The measured optical magnitudes at the location of AT 2023fhn (see Table A.4) allow a contribution from a point source with absolute magnitude as bright as ∼−14. A significant contribution from a point source at the location of AT 2023fhn is disfavoured (as the precise location has similar brightness to its immediate surroundings, as explained in Sect. 3.1), but the presence of a globular cluster or ultra-compact dwarf galaxy – which may host massive black holes (e.g. Seth et al. 2014) – cannot be ruled out. The presence of such an undetected cluster or ultra compact dwarf galaxy would be consistent with the upper limit on the black hole mass inferred from our late-time UV observations of $\lesssim 10^5$ M$_\odot$ (Mummery et al. 2024), given black hole – host galaxy/cluster mass relations (Kormendy & Ho 2013; Lützgendorf et al. 2013).

The UV-optical, X-ray and radio evolution of AT 2023fhn is broadly similar to other LFBOTs. Notably, however, the X-ray to UV luminosity ratio of AT 2023fhn is an order of magnitude lower than AT 2018cow at similar times, and up to 3

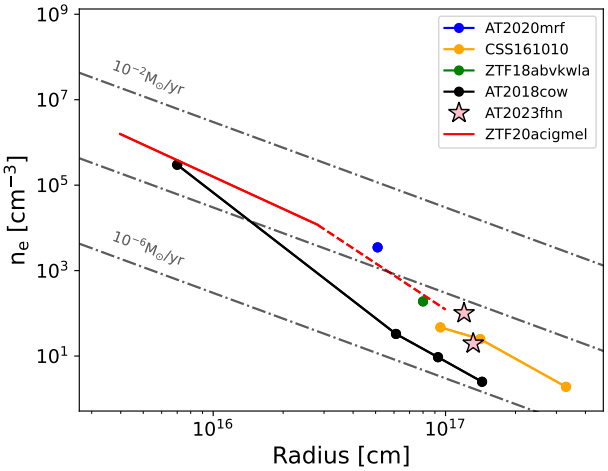

Fig. 11. Circumstellar density n_e at the radius of the shock R_p for AT 2023fhn and previous LFBOTs. The densities for ZTF 20 acigmel (Bright et al. 2022, Table 6) have been reduced by a factor ∼16 to align them with the equipartition $\epsilon_e = \epsilon_B = 1/3$ assumption used for all other measurements (for reference, see how Eq. (5) scales with ϵ_e and ϵ_B). As in Fig. 10, both AT 2023fhn epochs are shown, where the best constraints are from the epoch at 138 days. Other LBFOT results are from Ho et al. (2019; 2021, AT 2018cow), Ho et al. (2020, ZTF 18abvkwla), Coppejans et al. (2020, CSS161010), Bright et al. (2022, ZTF 20 acigmel, their fit to $n_e(r)$ is adopted, shown as a red solid/dash line either side of a possible break) and Yao et al. (2022, AT 2020mrf). Lines of constant $\dot{M}$ are shown for $v_w = 1000\,\mathrm{km\,s^{-1}}$. Note that due to different assumptions in the modelling, the densities and/or mass loss rates derived between different authors and objects can differ by up to a factor 5 (DeMarchi et al. 2022).

orders of magnitude lower than ZTF 20acigmel. As we show in Sect. 4.4, it is difficult to attribute this variety to differences in the circumstellar medium density or blast-wave propagation, as AT 2023fhn has a blast-wave velocity, energy and CSM comparable with other LFBOTs. This is consistent with the evidence from other LFBOTs thus far that the X-ray emission arises from a distinct mechanism, namely central engine activity. AT 2023fhn is only the third LFBOT with a mildly relativistic outflow ($v = 0.4^{+0.1}_{-0.2}c$), in common with CSS161010 and ZTF 18abvkwla, demonstrating that the blast wave is engine-driven. As can be seen in Fig. 11, all LFBOTs with sufficient constraints from radio observations thus far have a wind-like (in the sense that density decreases with distance), albeit not r^{-2}, circumstellar density profile. This suggests the CSM was produced by the progenitor system (i.e. through winds), rather than the explosion occurring in a pre-existing dense ISM, which would produce a flat density profile.

An alternative explanation for the variety in UV/X-ray ratios is the viewing angle, where the asymmetric outflow and accretion disc are being viewed from different angles. In this interpretation, the viewing angle to AT 2018cow was closer to perpendicular to the plane of the accretion disc (although not exactly perpendicular, Margutti et al. 2019). This conclusion was also reached by Maund et al. (2023) based on the high polarisation (and possibly for AT 2022tsd, given the observation of late-time optical flares Ho et al. 2023b). AT 2023fhn, meanwhile, would have been seen close to edge-on, well off-axis from any asymmetric outflow (e.g. from a choked jet) and with the inner accretion disc obscured (where choked jets and/or the inner disc dominates the X-ray luminosity, Jonker et al. 2020). The effect of viewing angle as an explanation for different LFBOT X-ray luminosities has also been posited by Metzger (2022) and Migliori et al. (2024).

With the fundamental LFBOT requirement of a low ^{56}Ni ejecta mass, and magnetar central engines struggling to explain all aspects of LFBOT phenomenology (e.g. the late-time emission in AT2018cow, Chen et al. 2023; Li et al. 2024), constraints on the possible progenitor models are tightening. IMBH TDE models remain plausible, if a dense wind-like CSM can be produced (e.g. by the ejection of stripped mass during the disruption event). However, the star-forming nature of the host galaxy population, and the locations of LFBOTs within them, likely disfavour such an interpretation. Other plausible models include the delayed merger of black holes and Wolf-Rayet stars (Metzger 2022), and failed supernovae (Quataert et al. 2019). In AT 2023fhn, the mass-loss wind parameter $A_\star \sim 1$ – higher than many radio loud supernovae (Chevalier & Fransson 2006) and collapsar GRBs (Gompertz et al. 2018; Chrimes et al. 2022). Such a dense circumstellar environment likely require a short-lived evolutionary stage with enhanced mass loss, for example pre-explosion winds from a blue supergiant or Wolf-Rayet star (Margutti et al. 2019).

6. Conclusions

We list here our conclusions about the nature of AT 2023fhn and its place in the context of other LFBOTs and extragalactic transients more generally.

1. Although relatively isolated compared with other LFBOTs and indeed most core-collapse supernovae, AT 2023fhn is otherwise consistent with a core-collapse event, associated with a typical star-forming galaxy and located in a young (albeit diffuse) stellar population.
2. The low X-ray to UV luminosity ratio demonstrates orders of magnitude of variety in this parameter among LFBOTs, which may be indicative of differences in viewing angle. In this interpretation, the relatively low X-ray luminosity of AT 2023fhn is due to an edge-on viewing angle, such that the inner accretion disc is obscured and we are well off-axis from any choked jet or asymmetric outflow.
3. The CSM properties are similar to previous LFBOTs, and are indicative of a dense surrounding medium. Given the wind-like n_e density profiles of other LFBOTs, and our n_e measurements of AT 2023fhn which continue this trend, it is likely that the dense CSM was produced by wind-like mass loss from the progenitor system itself (rather than the progenitor exploding in a pre-existing dense ISM).
4. An IMBH TDE interpretation remains possible only if there exists a pre-existing dense CSM or if the early stages of the tidal disruption produce such an environment. The host galaxy is likely undergoing tidal interactions, which may increase the chance of finding clusters (and hence TDEs) at high project offsets. While the non-nuclear location and host properties likely favour a core-collapse origin, the explosion of AT 2023fhn in an undetected globular cluster or ultra-compact dwarf galaxy cannot be ruled out.

Despite mounting evidence, the origin of LFBOTs is still ambiguous. Two approaches will elucidate which of the proposed scenarios contribute to the LFBOT population. The first is to grow the sample, enabling statistically robust comparisons of offsets and host galaxy properties to be made with other classes of transient. This will be possible with the advent of new wide-field, deep sky surveys such as those performed by the Vera Rubin observatory (Ivezić et al. 2019). The second is to perform detailed studies of future local events – such as AT2018cow – across the electromagnetic spectrum. Such events offer the best opportunity to search for underlying clusters, monitor the

long-term evolution, understand the detailed emission physics, and, ultimately, determine their progenitors. Although much progress has yet to be made, based on AT 2023fhn and the growing population of LFBOTs, we deem a massive star progenitor with strong winds but low ejecta mass to be the most likely scenario. This favours models such as the mergers of black holes and Wolf-Rayet stars or failed supernovae.

Acknowledgements. We thank the anonymous referee for their constructive feedback on this manuscript. A.A.C. acknowledges support from the European Space Agency (ESA) as an ESA Research Fellow. P.G.J. has received funding from the European Research Council (ERC) under the European Union's Horizon 2020 research and innovation program (Grant agreement No. 101095973). P.J.G. is partly supported by NRF SARChI Grant 111692. Observations analysed in this work were taken by the NASA/ESA Hubble Space Telescope under program 17238. This research has made use of software provided by the Chandra X-ray Center (CXC) in the application of the CIAO package (Fruscione et al. 2006). The National Radio Astronomy Observatory is a facility of the National Science Foundation operated under cooperative agreement by Associated Universities, Inc. Computing facilities were provided by the Scientific Computing Research Technology Platform of the University of Warwick. This research has made use of the Spanish Virtual Observatory (https://svo.cab.inta-csic.es) project funded by MCIN/AEI/10.13039/501100011033/ through grant PID2020-112949GB-I00. The Pan-STARRS1 Surveys (PS1) and the PS1 public science archive have been made possible through contributions by the Institute for Astronomy, the University of Hawaii, the Pan-STARRS Project Office, the Max-Planck Society and its participating institutes, the Max Planck Institute for Astronomy, Heidelberg and the Max Planck Institute for Extraterrestrial Physics, Garching, The Johns Hopkins University, Durham University, the University of Edinburgh, the Queen's University Belfast, the Harvard-Smithsonian Center for Astrophysics, the Las Cumbres Observatory Global Telescope Network Incorporated, the National Central University of Taiwan, the Space Telescope Science Institute, the National Aeronautics and Space Administration under Grant No. NNX08AR22G issued through the Planetary Science Division of the NASA Science Mission Directorate, the National Science Foundation Grant No. AST-1238877, the University of Maryland, Eotvos Lorand University (ELTE), the Los Alamos National Laboratory, and the Gordon and Betty Moore Foundation. This publication makes use of data products from the Wide-field Infrared Survey Explorer, which is a joint project of the University of California, Los Angeles, and the Jet Propulsion Laboratory/California Institute of Technology, funded by the National Aeronautics and Space Administration.

References

Avni, Y. 1976, ApJ, 210, 642
Barbary, K. 2016, https://doi.org/10.5281/zenodo.804967
Bright, J. S., Margutti, R., Matthews, D., et al. 2022, ApJ, 926, 112
Cendes, Y., Berger, E., Alexander, K. D., et al. 2024, ApJ, 971, 185
Chambers, K. C., Magnier, E. A., Metcalfe, N., et al. 2016, arXiv e-prints [arXiv:1612.05560]
Chen, Y., Drout, M. R., Piro, A. L., et al. 2023, ApJ, 955, 43
Chevalier, R. A. 1998, ApJ, 499, 810
Chevalier, R. A., & Fransson, C. 2006, ApJ, 651, 381
Chevalier, R. A., & Li, Z.-Y. 2000, ApJ, 536, 195
Chrimes, A. A., Gompertz, B. P., Kann, D. A., et al. 2022, MNRAS, 515, 2591
Chrimes, A. A., Jonker, P. G., Levan, A. J., et al. 2024, MNRAS, 527, L47
Conroy, C., & Gunn, J. E. 2010, ApJ, 712, 833
Conroy, C., Gunn, J. E., & White, M. 2009, ApJ, 699, 486
Conselice, C. J. 2003, ApJS, 147, 1
Coppejans, D. L., Margutti, R., Terreran, G., et al. 2020, ApJ, 895, L23
Dai, L., McKinney, J. C., Roth, N., Ramirez-Ruiz, E., & Miller, M. C. 2018, ApJ, 859, L20
DeMarchi, L., Margutti, R., Dittman, J., et al. 2022, ApJ, 938, 84
Dickey, J. M., & Lockman, F. J. 1990, ARA&A, 28, 215
DuPont, M., MacFadyen, A., & Zrake, J. 2022, ApJ, 931, L16
Eldridge, J. J., Stanway, E. R., Xiao, L., et al. 2017, PASA, 34, e058
Eldridge, J. J., Stanway, E. R., & Tang, P. N. 2019, MNRAS, 482, 870
Fitzpatrick, E. L. 1999, PASP, 111, 63
Foreman-Mackey, D. 2016, J. Open Source Softw., 1, 24
Foreman-Mackey, D., Hogg, D. W., Lang, D., & Goodman, J. 2013, PASP, 125, 306
Fox, O. D., & Smith, N. 2019, MNRAS, 488, 3772
Fragione, G., Leigh, N. W. C., Ginsburg, I., & Kocsis, B. 2018, ApJ, 867, 119
French, K. D., Arcavi, I., & Zabludoff, A. 2016, ApJ, 818, L21
Fruscione, A., McDowell, J. C., Allen, G. E., et al. 2006, SPIE Conf. Ser., 6270, 62701V
Gallazzi, A., Charlot, S., Brinchmann, J., White, S. D. M., & Tremonti, C. A. 2005, MNRAS, 362, 41
Gompertz, B. P., Fruchter, A. S., & Pe'er, A. 2018, ApJ, 866, 162
Gottlieb, O., Tchekhovskoy, A., & Margutti, R. 2022, MNRAS, 513, 3810
Granot, J., & Sari, R. 2002, ApJ, 568, 820
Hayasaki, K., & Jonker, P. G. 2021, ApJ, 921, 20
Ho, A. Y. Q. 2023, TNSAN, 174, 1
Ho, A. Y. Q., Phinney, E. S., Ravi, V., et al. 2019, ApJ, 871, 73
Ho, A. Y. Q., Perley, D. A., Kulkarni, S. R., et al. 2020, ApJ, 895, 49
Ho, A. Y. Q., Margalit, B., Bremer, M., et al. 2022, ApJ, 932, 116
Ho, A. Y. Q., Perley, D. A., Gal-Yam, A., et al. 2023a, ApJ, 949, 120
Ho, A. Y. Q., Perley, D. A., Chen, P., et al. 2023b, Nature, 623, 927
Ho, A. Y. Q., Liu, C., Andreoni, I., et al. 2023c, TNSAN, 93, 1
Ho, A. Y. Q., Bremer, M., Schulze, S., & Perley, D. 2023d, TNSAN, 100, 1
Hoffmann, S. L., Mack, J., Avila, R., et al. 2021, Am. Astron. Soc. Meet. Abstr., 53, 216.02
Inkenhaag, A., Jonker, P. G., Levan, A. J., et al. 2023, MNRAS, 525, 4042
Ivezić, Ž., Kahn, S. M., Tyson, J. A., et al. 2019, ApJ, 873, 111
Johnson, B. D., Leja, J., Conroy, C., & Speagle, J. S. 2021, ApJS, 254, 22
Johnson, B., Foreman-Mackey, D., Sick, J., et al. 2023, https://doi.org/10.5281/zenodo.10026684
Jonker, P. G., Stone, N. C., Generozov, A., van Velzen, S., & Metzger, B. 2020, ApJ, 889, 166
Kelly, P. L., & Kirshner, R. P. 2012, ApJ, 759, 107
Kennicutt, R. C., Jr., Tamblyn, P., & Congdon, C. E. 1994, ApJ, 435, 22
Khatami, D. K., & Kasen, D. N. 2024, ApJ, 972, 140
Kormendy, J., & Ho, L. C. 2013, ARA&A, 51, 511
Kron, R. G. 1980, ApJS, 43, 305
Kuin, N. P. M., Wu, K., Oates, S., et al. 2019, MNRAS, 487, 2505
Leja, J., Johnson, B. D., Conroy, C., van Dokkum, P. G., & Byler, N. 2017, ApJ, 837, 170
Li, L., Zhong, S.-Q., Xiao, D., et al. 2024, ApJ, 963, L13
Lützgendorf, N., Kissler-Patig, M., Neumayer, N., et al. 2013, A&A, 555, A26
Lyutikov, M., & Toonen, S. 2019, MNRAS, 487, 5618
Margutti, R., Metzger, B. D., Chornock, R., et al. 2019, ApJ, 872, 18
Martin, C., Barlow, T., Barnhart, W., et al. 2003, SPIE Conf. Ser., 4854, 336
Matthews, D., Margutti, R., Metzger, B. D., et al. 2023, Res. Notes Am. Astron. Soc., 7, 126
Maund, J. R., Höflich, P. A., Steele, I. A., et al. 2023, MNRAS, 521, 3323
Metzger, B. D. 2022, ApJ, 932, 84
Metzger, B. D., & Perley, D. A. 2023, ApJ, 944, 74
Migliori, G., Margutti, R., Metzger, B. D., et al. 2024, ApJ, 963, L24
Mummery, A., van Velzen, S., Nathan, E., et al. 2024, MNRAS, 527, 2452
Napolitano, N. R., Gatto, M., Spiniello, C., et al. 2022, A&A, 657, A94
Nayana, A. J., & Chandra, P. 2021, ApJ, 912, L9
Oke, J. B., & Gunn, J. E. 1982, PASP, 94, 586
Pasham, D. R., Ho, W. C. G., Alston, W., et al. 2021, Nat. Astron., 6, 249
Pellegrino, C., Howell, D. A., Vinkó, J., et al. 2022, ApJ, 926, 125
Perley, D. A., Mazzali, P. A., Yan, L., et al. 2019, MNRAS, 484, 1031
Perley, D. A., Ho, A. Y. Q., Yao, Y., et al. 2021, MNRAS, 508, 5138
Petrosian, V. 1976, ApJ, 210, L53
Prentice, S. J., Maguire, K., Smartt, S. J., et al. 2018, ApJ, 865, L3
Quataert, E., Lecoanet, D., & Coughlin, E. R. 2019, MNRAS, 485, L83
Rivera Sandoval, L. E., Maccarone, T. J., Corsi, A., et al. 2018, MNRAS, 480, L146
Rodrigo, C., & Solano, E. 2020, XIV.0 Scientific Meeting (virtual) of the Spanish Astronomical Society, 182
Rodrigo, C., Solano, E., & Bayo, A. 2012, SVO Filter Profile Service Version 1.0, IVOA Working Draft 15 October 2012, 1015
Rodriguez-Gomez, V., Snyder, G. F., Lotz, J. M., et al. 2019, MNRAS, 483, 4140
Schlafly, E. F., & Finkbeiner, D. P. 2011, ApJ, 737, 103
Schrøder, S. L., MacLeod, M., Loeb, A., Vigna-Gómez, A., & Mandel, I. 2020, ApJ, 892, 13
Schulze, S., Yaron, O., Sollerman, J., et al. 2021, ApJS, 255, 29
Seth, A. C., van den Bosch, R., Mieske, S., et al. 2014, Nature, 513, 398
Soderberg, A. M., Kulkarni, S. R., Berger, E., et al. 2005, ApJ, 621, 908
Soker, N. 2022, Res. Astron. Astrophys., 22, 055010
Stanway, E. R., & Eldridge, J. J. 2018, MNRAS, 479, 75
Sun, N.-C., Maund, J. R., Crowther, P. A., & Liu, L.-D. 2022, MNRAS, 512, L66
Sun, N.-C., Maund, J. R., Shao, Y., & Janiak, I. A. 2023, MNRAS, 519, 3785
Tonry, J. L., Stubbs, C. W., Lykke, K. R., et al. 2012, ApJ, 750, 99
Tremonti, C. A., Heckman, T. M., Kauffmann, G., et al. 2004, ApJ, 613, 898
Uno, K., & Maeda, K. 2020, ApJ, 897, 156
Xiang, D., Wang, X., Lin, W., et al. 2021, ApJ, 910, 42
Yao, Y., Ho, A. Y. Q., Medvedev, P., et al. 2022, ApJ, 934, 104
Zhang, W., Shu, X., Chen, J.-H., et al. 2022, Res. Astron. Astrophys., 22, 125016

Appendix A: Additional tables

Table A.1. Details of all *Chandra* observations of AT 2023fhn from program 24500143 (PI: Chrimes).

ObsID	Start date JD-2460045	t_{exp} ks	Data mode	F_X erg s^{-1} cm^{-2}
26624	14.78957	29.68	FAINT	$(7.6^{+2.2}_{-1.8})\times10^{-15}$
26625	27.98310	29.68	FAINT	$(4.5^{+4.7}_{-2.9})\times10^{-16}$
27833	29.47145	29.67	FAINT	
26626	61.80356	16.88	VFAINT	
27895	62.33516	10.94	VFAINT	
27835	65.12251	13.89	FAINT	$< 8.2 \times 10^{-16}$
27905	65.45429	13.89	FAINT	
27906	65.79704	13.89	FAINT	
27907	66.13969	13.89	FAINT	
26627	198.66317	10.74	VFAINT	
28997	198.96634	10.74	VFAINT	
28998	199.27127	11.12	VFAINT	
27837	205.89744	13.4	VFAINT	
29031	206.23509	13.3	VFAINT	
29032	206.57170	13.5	VFAINT	
29034	207.96147	10.93	VFAINT	
29033	208.26639	14.39	VFAINT	$< 3.5 \times 10^{-16}$
27838	215.80840	16.85	VFAINT	
29054	216.19957	17.84	VFAINT	
29056	216.60163	14.39	VFAINT	
28991	218.76822	9.94	VFAINT	
28999	219.12318	18.69	VFAINT	
29055	219.54352	16.85	VFAINT	

Notes. ObsID, exposure start times (since JD-2460045) and data mode are listed. All observations are made with ACIS-S. The fluxes F_X are unabsorbed and measured in the energy range 0.5-7.0 keV. Individual observations in each of the four epochs are merged as indicated. Uncertainties are given at 1σ, upper limits at 2σ.

Table A.2. Details of all HST data for AT 2023fhn, from program 17238 (PI: Chrimes).

Filter	Start date JD–2460045	t_{exp} s
F555W	36.87666	1092
F814W	36.89272	1092
F555W	196.42824	990
F814W	196.44313	1092
F225W	196.49431	1068
F336W	196.51027	1068
F845M	196.56034	990
F763M	196.57515	1068

Notes. Filter, exposure start times (JD-, where is 12:00 UT on 10-APR-2023) and exposure durations t_{exp} are given. All observations are with WFC3 in the UVIS channel.

Table A.3. AT 2023fhn radio flux densities from our VLA program (SC240143, PI: Chrimes).

Start date JD–2460045	Freq. GHz	Bandwidth GHz	t_{exp} min.	Flux Density μJy/beam
11.80740	1.52	1.024	38	<130
11.78309	3.00	2.048	32	<35
11.76507	6.00	4.096	23	<18
11.74688	10.00	4.096	23	<18
11.72090	15.08	6.144	35	<11
11.69229	22.00	8.192	35	<17
11.66552	33.00	8.192	33	<25
87.59185	1.52	1.024	39	<45
87.56657	3.00	2.048	33	110±8
87.54257	6.00	4.096	32	128±5
95.58690	10.00	4.096	31	105±7
95.56438	15.00	6.144	30	71±7
95.52738	22.00	8.192	47	60±10
137.17440	1.52	1.024	39	<58
137.14178	3.00	2.048	44	110±10
137.10567	6.00	4.096	50	221±5
138.16972	10.00	4.096	42	197±6
138.13664	13.00	2.050	42	180±10
138.13664	15.00	2.050	42	160±10
138.13664	16.96	2.050	42	140±20
249.95139	6.00	4.096	35	<311[a]
249.90997	10.00	4.096	57	<181[a]
249.86861	15.08	6.144	57	<125[a]

Notes. Observation start times are listed with respect to JD–2460045 (12:00 on 10-Apr-2023). The quoted uncertainties do not include the systematic uncertainty of 5% on the absolute flux calibration at these frequencies. Upper limits are given as 3 times the local RMS. [a]The resolution of the last three observations was lower (as the VLA was in D configuration at the time), so we could not remove contaminating sources at the target location and have consequently listed the upper limit as the flux density at the source location.

Table A.4. HST magnitudes m, and their uncertainties δm, for the second epoch of AT 2023fhn imaging at ~ 200 days (see Table A.2).

Filter	Method	Bkg.	Aper.	m	δm
F225W	PHOTUTILS	Median	0.2″	>26.1	-
F225W	PHOTUTILS	Annulus	0.2″	>26.1	-
F225W	PHOTUTILS	Median	0.4″	>25.4	-
F225W	PHOTUTILS	Annulus	0.4″	>25.5	-
F336W	PHOTUTILS	Median	0.2″	>26.6	-
F336W	PHOTUTILS	Annulus	0.2″	>26.6	-
F336W	PHOTUTILS	Median	0.4″	>25.9	-
F336W	PHOTUTILS	Annulus	0.4″	>25.9	-
F555W	PHOTUTILS	Median	0.2″	26.9	0.2
F555W	PHOTUTILS	Annulus	0.2″	27.1	0.3
F555W	PHOTUTILS	Median	0.4″	25.8	0.2
F555W	PHOTUTILS	Annulus	0.4″	25.6	0.1
F763M	PHOTUTILS	Median	0.2″	>26.0	-
F763M	PHOTUTILS	Annulus	0.2″	>26.0	-
F763M	PHOTUTILS	Median	0.4″	>25.3	-
F763M	PHOTUTILS	Annulus	0.4″	25.0	0.3
F814W	PHOTUTILS	Median	0.2″	26.4	0.2
F814W	PHOTUTILS	Annulus	0.2″	26.5	0.3
F814W	PHOTUTILS	Median	0.4″	25.3	0.2
F814W	PHOTUTILS	Annulus	0.4″	25.2	0.2
F845M	PHOTUTILS	Median	0.2″	>25.6	-
F845M	PHOTUTILS	Annulus	0.2″	>25.6	-
F845M	PHOTUTILS	Median	0.4″	>24.9	-
F845M	PHOTUTILS	Annulus	0.4″	>24.9	-

Notes. Upper limits are given at 3σ. In all six filters, two photometry methods are listed - aperture photometry with median background estimation, and aperture photometry with annulus background estimation. Two aperture sizes (and hence enclosed energy corrections) are given in each case.

Appendix B: SED fitting MCMC results

In this appendix we provide the joint posterior parameter distributions for the host galaxy of AT 2023fhn, in the form of a corner plot (Fig. B.1) including stellar mass, metallicity, extinction, population age and timescale for an exponentially declining star formation history. These are provided as outputs from EMCEE SED-fitting using PROSPECTOR. For the MCMC initial values (and flat priors) we use $A_V = 0.05$ ($0<A_V < 2$), $t_{age} = 1$ Gyr and M= 10^{10} $M_\odot$ (10^6 <M/$M_\odot$ < 10^{12}), with a flat prior on τ of $0.1 < \tau$/Gyr<100. For our fiducial run, the redshift is fixed at $z = 0.238$ and the metallicity at $Z = 0.5Z_\odot$. Also provided in Table B.1 are results when Z is allowed to vary as a free parameter.

Table B.1. Host galaxy properties derived from PROSPECTOR SED fitting, as in Table 2, but allowing the metallicity Z to vary.

Host property	Value
$M_\star$ / $M_\odot$	$(1.21\pm0.08) \times 10^{10}$
SFR / $M_\odot$ yr^{-1}	$8.8^{+1.3}_{-1.1}$
$Z/Z_\odot$	0.08 ± 0.02
A_V	$0.47^{+0.06}_{-0.06}$
t_{age}/Gyr	$1.9^{+0.3}_{-0.4}$
τ/Gyr	$1.1^{+1.2}_{-0.6}$

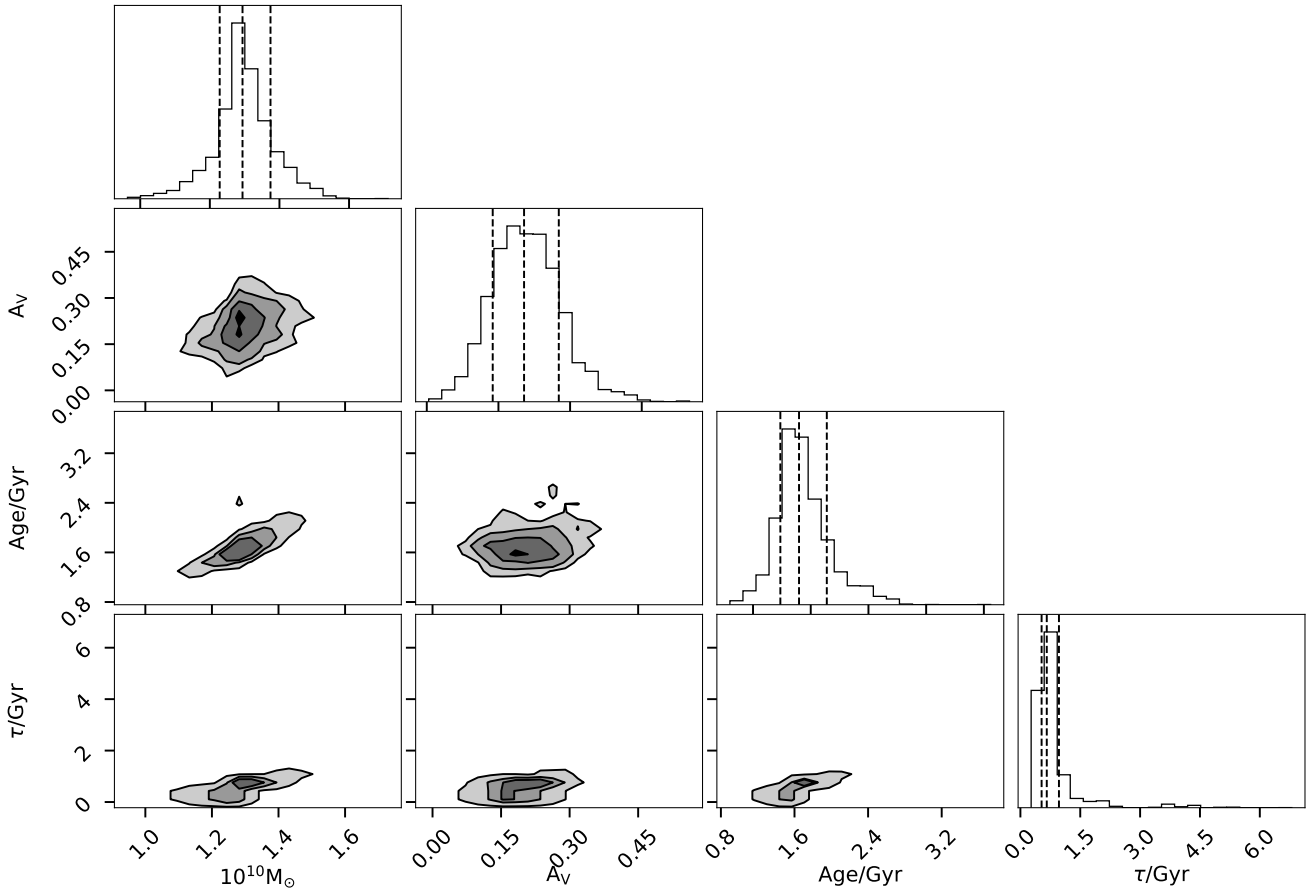

Fig. B.1. EMCEE output from PROSPECTOR for the host of AT 2023fhn. Produced using the CORNER.PY code (Foreman-Mackey 2016) via PROSPECTOR. The metallicity is fixed at $0.5Z_{\odot}$.